Title
Theoretical detection threshold of the proton-acoustic range verification technique

Journal
Medical Physics, 42(10)

ISSN
0094-2405

Authors
Ahmad, Moiz
Xiang, Liangzhong
Yousefi, Siavash
et al.

Publication Date
2015-09-09

DOI
10.1118/1.4929939

Peer reviewed

Theoretical detection threshold of the proton-acoustic range verification technique

Moiz Ahmad
Department of Radiation Oncology, Stanford University School of Medicine, Stanford, California 94305-5847

Liangzhong Xiang
Center for Bioengineering and School of Electrical and Computer Engineering, University of Oklahoma, Norman, Oklahoma 73019-1101

Siavash Yousefi and Lei Xing[a)]
Department of Radiation Oncology, Stanford University School of Medicine, Stanford, California 94305-5847

(Received 10 May 2015; revised 17 July 2015; accepted for publication 19 August 2015; published 9 September 2015)

Purpose: Range verification in proton therapy using the proton-acoustic signal induced in the Bragg peak was investigated for typical clinical scenarios. The signal generation and detection processes were simulated in order to determine the signal-to-noise limits.
Methods: An analytical model was used to calculate the dose distribution and local pressure rise (per proton) for beams of different energy (100 and 160 MeV) and spot widths (1, 5, and 10 mm) in a water phantom. In this method, the acoustic waves propagating from the Bragg peak were generated by the general 3D pressure wave equation implemented using a finite element method. Various beam pulse widths (0.1–10 μs) were simulated by convolving the acoustic waves with Gaussian kernels. A realistic PZT ultrasound transducer (5 cm diameter) was simulated with a Butterworth bandpass filter with consideration of random noise based on a model of thermal noise in the transducer. The signal-to-noise ratio on a per-proton basis was calculated, determining the minimum number of protons required to generate a detectable pulse. The maximum spatial resolution of the proton-acoustic imaging modality was also estimated from the signal spectrum.
Results: The calculated noise in the transducer was 12–28 mPa, depending on the transducer central frequency (70–380 kHz). The minimum number of protons detectable by the technique was on the order of $3–30\times10^6$ per pulse, with 30–800 mGy dose per pulse at the Bragg peak. Wider pulses produced signal with lower acoustic frequencies, with 10 μs pulses producing signals with frequency less than 100 kHz.
Conclusions: The proton-acoustic process was simulated using a realistic model and the minimal detection limit was established for proton-acoustic range validation. These limits correspond to a best case scenario with a single large detector with no losses and detector thermal noise as the sensitivity limiting factor. Our study indicated practical proton-acoustic range verification may be feasible with approximately 5×10^6 protons/pulse and beam current. [http://dx.doi.org/10.1118/1.4929939]

Key words: proton acoustics, proton therapy, range verification

1. INTRODUCTION

The treatment accuracy of current proton and ion therapy is limited by the proton range uncertainty, which may adversely affect patient outcomes. There is a sharp accumulation of radiation dose at the distal end of the particle range (i.e., the Bragg peak). Therefore, small changes in the proton range can severely underdose the target volume and excessively overdose adjacent critical organs.[1] The range uncertainty contributes to an increase in the planned treatment volume (PTV). Thus, minimizing the uncertainty in the proton range is a problem of great interest in proton and ion therapy. Remote measurement of the Bragg peak position is especially challenging considering that all protons in the treatment beam are absorbed inside patient, leaving no means of monitoring dose via proton detectors. Proton range verification methods include PET (Ref. 2) and prompt gamma imaging.[3,4] These methods require inferring proton dose from a spatial distribution of nuclear emissions which follows a complex, nonlinear relationship. Finally, the PET method is not real-time, and therefore may not be used to adjust a treatment session as it occurs.

Acoustic signals produced by radiation traversing matter have been previously investigated in nuclear physics as a means for accelerator beam monitoring[5] and in astrophysics for cosmic particle detection.[6] These methods were subsequently proposed in radiation oncology for verification of proton and ion therapy[7,8] and at least one instance of a proton-acoustic signal in a patient study has been recorded.[9] Additionally, x-ray induced acoustic imaging has been demonstrated as a feasible method for imaging spatially varying dose distributions.[10] The physical mechanism underlying the proton-acoustic method is the thermoelastic pressurization of matter upon proton irradiation, which is the same underlying

physical mechanism as that in photoacoustic imaging.[11] A short pulse of proton radiation causes an instantaneous local increase in temperature and pressure. The local pressure rise travels outward in the form of ultrasonic pressure waves that are subsequently detected by ultrasound transducer detectors. The arrival time of the detected ultrasound pulse relative to the time of the proton irradiation pulse is directly proportional to the distance from the Bragg peak to the ultrasound detector. This provides the basis of localizing the Bragg peak within the patient. Studies by Jones *et al.* and Alsanea *et al.* indicate that Bragg peak localization with about 1-mm precision may be possible.[12,13] These studies also showed that the use of multiple ultrasound detectors may reconstruct a tomographic image of the proton dose distribution.

The proton-acoustic method of verifying proton dose offers several advantages. First, it provides real-time feedback, allowing intratreatment adjustment. Second, spatial resolution in ultrasound imaging is generally better than in nuclear imaging methods; thus, it may better reduce proton range uncertainty. Finally, ultrasonic instrumentation is generally much less expensive than nuclear imaging instrumentation.

Proton-acoustic signal depends on a variety of parameters such as the beam pulse width, energy, spot size, and measurement noise. The limits of proton-acoustic detection are currently not well understood. Given the recent attention to proton and ion-acoustics research,[12,14–16] we investigate the detection limits on proton-acoustic signals in clinical proton therapy scenarios. The sensitivity of proton-acoustic imaging is ultimately limited by thermal noise within the ultrasound transducers.[17,18] By deriving the noise from fundamental physical principles, we determine the detection threshold of the proton-acoustic method. These results set the limit on the sensitivity of the proton-acoustic method and should establish a quick reference for assessing whether a given irradiation scenario produces a detectable proton-acoustic signal. Finally, we report the frequency and bandwidth of the proton-acoustic signals. These features inform the selection of transducers in proton-acoustics applications.

2. METHODS

2.A. Proton dose distribution

The semiempirical analytical model presented by Pedroni *et al.*[19] was used to calculate the dose distribution (per proton) for beams of different energy and spot widths. This model has demonstrated a dosimetric accuracy of 1%–2% compared to measurements over a wide range of energies, field sizes, and field shapes. The advantage of this model over other approaches such as Monte Carlo simulation is its computational simplicity and accuracy over a wide range of proton beam parameters. In this model, the dose D due to a single proton at a depth w and transverse distance x and y for a proton beam with energy E is

$$D(x,y,w,E) = T(w,E) \times G(x,\sigma_x(w,E)) \times G\big(y,\sigma_y(w,E)\big). \quad (1)$$

D is the statistically averaged dose per proton over an irradiation with many protons, where $T(w,E)$ is a semiempirical depth-dose factor whose values have been previously tabulated. The tabulated values of T used the theoretical Bethe-Bloch proton stopping power formula to calculate the proton energy loss vs depth from fundamental principles and incorporated empirical data to fit functions that include the effects of range straggling and nuclear interactions. $G(x,w,\sigma_x(w),E)$ and $G(y,w,\sigma_y(w),E)$ are normal (Gaussian) functions that characterize the transverse dose distribution in the x and y directions, respectively. They have a mean value of zero and the widths $\sigma_x(w)$ and $\sigma_y(w)$ characterize the lateral spread of the beam with depth. $\sigma_x(w)$ and $\sigma_y(w)$ were found by fitting a parameterized function representing accumulated Coulomb scattering with depth to measurements of lateral beam spreading. $\sigma_x(w)$ and $\sigma_y(w)$ are semiempirical factors and we used tabulated values of $\sigma_x(w)$ and $\sigma_y(w)$ in our simulations.

2.B. Initial pressurization and acoustic propagation

The energy deposited by the proton beam is considered instantaneous leading to an instantaneous rise in pressure. The initial local pressure rise P_0 is assumed to be proportional to the energy density deposited and the proportion is given by the Grüneisen parameter Γ,

$$P_0 = \Gamma E = \Gamma \rho D, \quad (2)$$

where E is the local energy density (in J/m^3). Γ is a dimensionless quantity and a value of $\Gamma = 0.15$ has been measured for soft at physiological temperature and atmospheric pressure.[20] Although Γ varies with both temperature and pressure, we are concerned with only small temperature and pressure rises here, and the variation in the Grüneisen parameter Γ is thus negligible. The energy density is equal to the dose D multiplied by the material density ρ, approximately $\rho = 1000$ kg/m^3 in soft tissue.

The initial local pressure at the proton Bragg peak produces pressure waves carrying the thermoelastic energy away. The pressure field p_i at any point r and at time t can be calculated by solving the general wave equation,

$$\left(\nabla^2 - \frac{1}{v_s^2}\frac{\partial^2}{\partial t^2}\right) p_i(r,t) = 0, \quad (3)$$

subject to the initial condition, $p_i(r,0) = P_0$. The solution p_i is the resulting acoustic field due to an infinitesimal-width impulse of the proton beam. In practice, the solution is valid as long as the pulse width is shorter than the thermal confinement time in the media. v_s is the speed of sound in the acoustic medium (v_s is approximately 1500 m/s in soft tissue).

We solve the equations iteratively using the k-space pseudospectral finite element method.[21] Briefly, this method computes the finite difference derivatives $(\partial/\partial x, \partial/\partial y, \partial/\partial z, \partial/\partial t)$ in the frequency domain. The advantage of transforming the pressure field into the frequency domain is that fewer grid points are required for an accurate solution. The k-space pseudospectral finite element method has been previously implemented in MATLAB (Mathworks, Natick, MA) by the group of Treeby and Cox in the k-Wave MATLAB toolbox[21] and has been used extensively in many acoustic simulation studies. We provided the initial condition P_0 and the field locations

r as inputs into k-Wave which calculated the output pressure waveform $p_i(t)$ at field point r. The wave propagation at each time step also incorporates the attenuation of soft tissue, by using a power-law exponential attenuation with attenuation coefficient of 0.75 dB/(MHz$\hat{}y$ cm) and exponent $y = 1.5$.

$p_i(t)$ the impulse response of the acoustic field due to a short, intense pulse of the proton beam. As long as the condition of acoustic stress confinement is satisfied, the temporal shape of the pulse does not matter. This means the accumulated pressure does not dissipate away during the irradiation if the pulse is sufficiently short. The stress confinement time T for tissue is given by $T = \delta/v$, where δ is the radiation penetration depth or spot size and v is the speed of sound in the medium. Taking the width of the Bragg peak to be approximately $\delta = 1$ cm, the stress confinement time is approximately 6 μs. To find the response to proton pulse widths on this scale or longer, we simply convolve the impulse response with the excitation pulse temporal profile $G(t,0,\sigma_t)$, where G is a normalized Gaussian function with mean 0 and standard deviation σ_t. The pulse width is the full-width half maximum of G and is equal to $2.35\sigma_t$. The pressure field due to a proton pulse with width σ_t is thus

$$p(t) = p_i(t) \otimes G(t,0,\sigma_t). \tag{4}$$

In effect, this is equivalent to dividing the proton beam impulse into smaller excitation pulses spread over a time period of σ_t and then summing the resulting fields from these impulses. This convolution operation is valid because of the linearity of Eq. (4) in both space and time.

$p(r,t)$ in Eq. (4) is the *actual* pressure waveform at field point r independent of any detector. The *measured* signal is dependent on the transducer bandwidth. In principle, an infinite bandwidth will preserve the shape and intensity of the acoustic waveform; however, noise also increases with bandwidth. Thus, there is a trade-off between high measurement accuracy with a wide bandwidth detector and low noise with a low bandwidth detector. The transducer acts as a bandpass filter on the actual pressure waveform. We simulate this effect by filtering $p_i(t)$ with a Butterworth bandpass filter. Briefly, the effect of this filter is approximately that of an ideal bandpass filter (i.e., *rect* function): all frequencies in $f(t)$ below f_{low} and above f_{high} are reduced to zero amplitude, while the band of frequencies between f_{low} and f_{high} has a gain of 1. It is known that the sharp discontinuities in the ideal bandpass filter result in unrealistic ringing artifacts; therefore, we used the Butterworth filter instead to avoid these ringing artifacts. Notationally, we represent the filtering operation as

$$p'(t) = B\left(p_i(t), f_{\text{low}}, f_{\text{high}}\right), \tag{5}$$

where $B(f(t),f_{\text{low}},f_{\text{high}})$ is the signal $f(t)$ after it is filtered by the first order Butterworth bandpass filter with lower and upper cutoff frequencies f_{low} and f_{high}, respectively. The filter response at f_{low} and f_{high} is exactly half (−3 dB) compared to f_{max}, which is approximately equal to the central frequency $f_{\text{cent}} = (f_{\text{high}} + f_{\text{low}})/2$. The spectrum of the acoustic signal decreases with frequency. The cutoff frequency f_{high} was chosen such that the amplitude of the spectrum (Fourier transform magnitude) at f_{high} is equal to the noise amplitude: i.e., frequencies above f_{high} cannot be detected against the noise. Once f_{high} is chosen, f_{low} is set as $f_{\text{high}}/3$. This sets the bandwidth $(f_{\text{high}} - f_{\text{low}})$ equal to $100\% * f_{\text{cent}}$ (100% bandwidth). Bandwidth of 100% is a typical bandwidth of wideband piezo-electric ultrasound transducers.

2.C. Noise model

The dominant source of noise in low intensity ultrasound applications is thermal noise inside piezoelectric element of the ultrasound transducer. This is widely acknowledged as the dominant noise source in the wider thermoacoustics literature.[17,18] Hayakawa *et al.* noted that electronic noise interfered with their proton-acoustic measurements.[9] However, in the Appendix we make calculations of electronic noise from amplifier circuits and show that it is negligible in comparison with the transducer thermal noise when low-noise amplifiers are used to amplify the signal immediately after transduction. The noise-equivalent pressure (noise in units of pressure) is given by

$$N = \frac{1}{gl}\sqrt{\frac{4kT}{C}}, \tag{6}$$

where k is Boltzmann's constant, and T is the absolute temperature of the transducer. C, g, and l are the capacitance, piezoelectric modulus, and thickness, respectively, of the piezoelectric element of the transducer. The square-root term represents voltage noise due to thermal fluctuations in capacitance C. The product gl is the sensitivity of the transducer (e.g., in volts per pascal). From the definition above, the following expression for N can be derived:[17]

$$N = \sqrt{\frac{9.2kT}{c_l \epsilon \epsilon_0 g^2 A} f_{\text{max}}}. \tag{7}$$

A is the surface area of the piezomaterial and f_{max} is the maximum detectable frequency of the transducer. c_l and $\varepsilon\varepsilon_0$ are the speed of sound and dielectric permittivity of the piezoelectric material, respectively. From Eq. (7), it is seen that noise depends on the following factors: (1) temperature, (2) the product $\eta = c_l \epsilon \epsilon_0 g^2$, which is an intrinsic quantity of the piezoelectric material, (3) A and f_{max}, which depend on the physical dimensions of the piezo element. The paper by Oraevsky and Karabutov[17] lists the value of η for different materials: lithium niobate, quartz, lead zirconate titanate (PZT), and polyvinyldenefluoride (PVDF). Of these materials, PZT has the highest piezo-electric efficiency ($\eta = 27 \times 10^{-9}$ m^3/s N, which is seven times greater than any of the other materials). PZT is preferred for many wideband ultrasound applications below 2 MHz.[17] Therefore, we set the value of η to that of PZT. The most sensitive detectors are hydrophones with PZT transducer elements, and we have assumed a submerged PZT hydrophone in this simulation study.

Equation (7) can be written as $N = N_0\sqrt{f_{\text{max}}}$, where N_0 is the noise spectral density. Assuming a PZT transducer with a 5 cm diameter ($A = 20$ cm^2) and a value of $\eta = 27 \times 10^{-9}$ m^3/s

N for PZT and room temperature of 296 K, we calculated a value of $N_0 = 2.7 \times 10^{-5}$ Pa/$\sqrt{\text{Hz}}$ for the noise spectral density of our transducer model. This is within the range of transducer noise spectral density values for a wide variety of transducers listed by Winkler *et al.*[18] Given the large area of the transducer and the assumption of no other noise sources, this should be considered a reasonable minimum noise floor for a PZT transducer. Although one can enhance sensitivity with multiple detectors, we focus here on proton-acoustic detection with a single-element transducer for simplicity.

For the calculation of N according to Eq. (7) in each of the simulations, we set $f_{\max}$ equal to the maximum frequency present in the acoustic signal: i.e., $f_{\max}$ is set to the frequency at which the Fourier transform of the signal decreases below the noise spectral density N_0. We generated random noise ϵ at each time point in the acoustic waveform by sampling a Gaussian probability distribution. The noisy *measured* signal $p_{\text{proton}}(t)$ in the simulation was thus calculated as

$$p_{\text{proton}}(t) = p'(t) + \epsilon \sim G(0,N), \tag{8}$$

where ϵ is a Gaussian random variable with mean 0 and standard deviation N. This represents an average acoustic signal on a per-proton basis.

We defined the per-proton SNR as the ratio of the noiseless signal $p'(t)$ peak value to the noise intensity N,

$$\text{SNR} = \frac{\max(p'(t))}{N}. \tag{9}$$

To determine the minimum detectable dose, we multiplied the per-proton dose by the ratio 4/SNR,

$$D_{\text{det}} = D(0,0,d_{\max},E)\frac{4}{\text{SNR}}, \tag{10}$$

where $D(0,0,d_{\max},E)$ is the dose per proton at the Bragg peak for a proton beam with energy E. This value of 4 for the target SNR is based on the widely accepted Rose criterion for minimum SNR in signal processing.[22]

2.D. Evaluation cases

We consider two different clinical proton therapy scenarios: (i) a deep seated target. This represents a common prostate cancer in a male adult; the target is treated with a 160 MeV proton beam with a maximum dose depth of 17.2 cm, (ii) a tumor at a shallower depth, such as in a pediatric patient. The target is treated with a 100 MeV proton beam with a maximum dose depth of 7.5 cm. For both scenarios we considered fields with 1, 5, and 10 mm spot sizes.

3. RESULTS

Figure 1 displays the average dose distribution per proton for two beams: 100 and 160 MeV with a 5-mm spot size. Each proton delivers a statistically averaged dose on the order of several nGy at the Bragg peak. For each beam, the detector was located 4-cm distal to the Bragg peak. Figures 2 and 3 depict the simulated acoustic signals in the time-domain and frequency-domain, respectively. For the purpose of illustration, we have chosen to display the results for the 100-MeV beam with the 1-mm spot beam.

Figure 2 (left) shows both the actual field pressure $p(t)$ and the simulated measured signal $p_{\text{pulse}}(t)$ for a 0.1-μs pulse with a 235-mGy dose. The acoustic pulse arrives approximately 26 μs after irradiation, indicating a detector distance of 40 mm distal to the Bragg peak. The absolute pressures (on the order

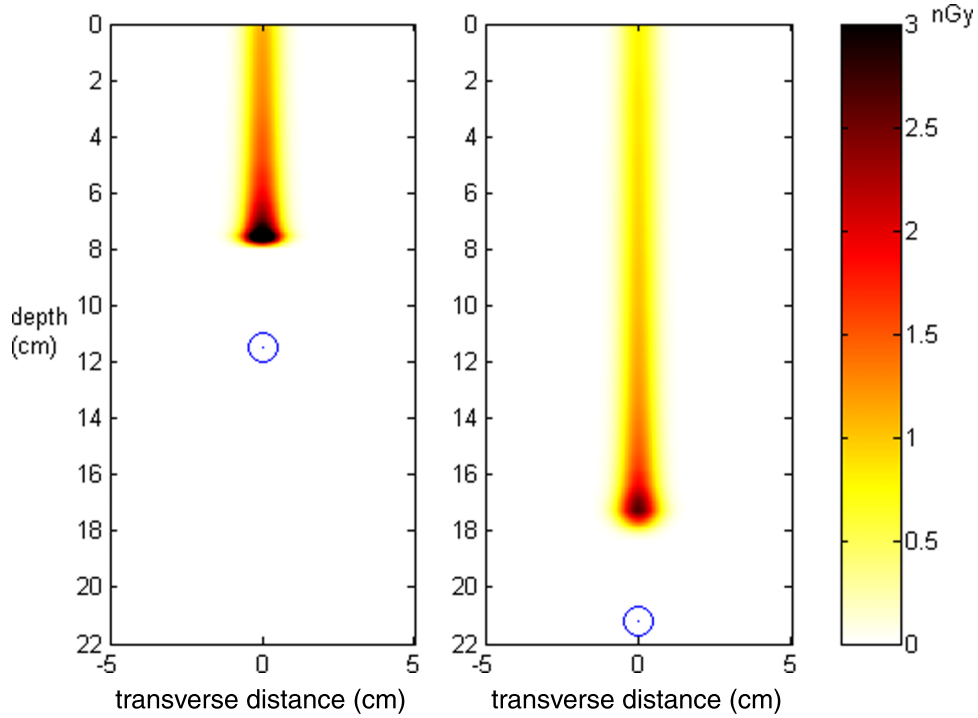

FIG. 1. Dose distributions for the 100 MeV (left) and 160 MeV (right) beams. The dose values are the average dose per proton. The blue circular marker indicates the position of the detector (4 cm distal to the Bragg peak in each case).

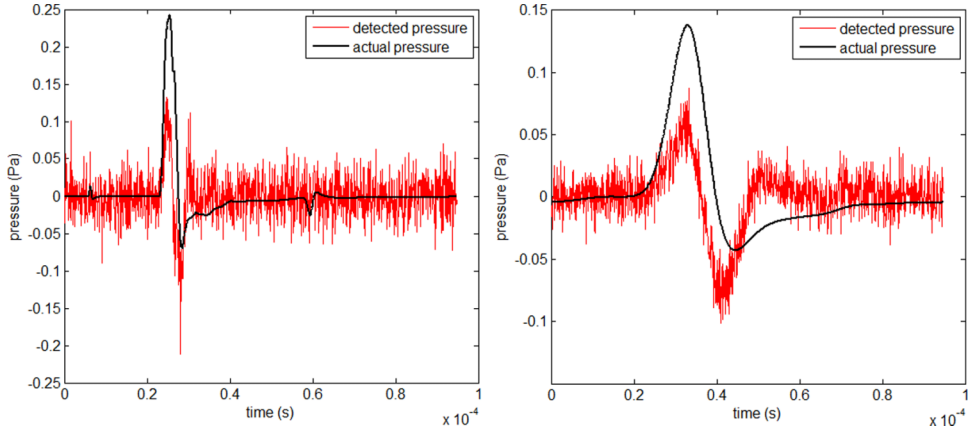

FIG. 2. Simulated acoustic waveforms at a detector 4 cm from the Bragg peak of the proton beam. The beam had a 100-MeV energy and a 1-mm spot size. Left: waveform for a beam with a 0.1-μs pulse width (235 mGy/pulse). Right: beam with a 10-μs pulse width (647 mGy/pulse). "Actual pressure" refers to the waveform detected by an ideal noiseless detector with infinite bandwidth. "Detected pressure" refers to the waveform measured by the realistically modeled transducer.

of 100 mPa) are indicated on the vertical axis. The narrow pulse width relates to a 1-mm spatial resolution. The second pulse (in the actual pressure waveform) that arrives after the main pulse is from the phantom entrance (zero depth relative to the proton beam); however, this secondary pulse cannot be detected because it is much smaller than the detector noise. Figure 2 (right) also shows the acoustic waveform for a 10-μs pulse with a 647 mGy dose. The actual peak pressure is also lower: 140 mPa for the 10-μs pulse compared to 250 mPa for the 0.1-μs pulse, despite the higher dose and lower noise. This is due to temporal widening of the signal, which also leads to lower acoustic peak amplitudes. The spectrum was calculated by taking the magnitude of the Fourier transform of the acoustic waveform: $P(f) = |\Im\{p(t)\}|$. For the beam with the 0.1-μs pulse width, it is apparent that most of the signal energy is concentrated around 60 kHz, with a second lobe around 400 kHz (Fig. 3, left). Most of the signal energy is concentrated at low frequencies; however, the useful spatial information comes from the high frequencies. The spectrum for the 0.1-μs beam contains signal at frequencies past 1 MHz, but with diminishing amplitude. Therefore, the measurements with high-frequency transducers requires increasingly higher dose per pulse. When the pulse width is increased from 0.1- to 10-μs, the maximum frequency decreases from around 500 to 100 kHz (Fig. 3, right). At this low frequency, the signal is centered around 76 kHz. For pulse widths wider than 10-μs, the signal will shift to even lower frequencies, which will make it difficult to localize the acoustic pulse in time with high precision.

Tables I and II show the minimum requirements in terms of dose and number of protons for each of the scenarios in this study. We also list the highest achievable spatial resolution based on the spectral content of the acoustic signal. Here are a few general observations regarding the results as a whole: the required doses (at the depth of maximum dose) are on the order of 50–500 mGy/pulse. The corresponding number of protons is on the order of $2\text{–}20\times10^6$ per pulse. There are also several identifiable trends in these data. First, as the pulse width increases, the spectrum (indicated in Tables I and II by the central frequency) shifts to lower frequencies. This was depicted in Fig. 3. Second, as the beam spot size increases, the minimum number of protons also increases. This is due

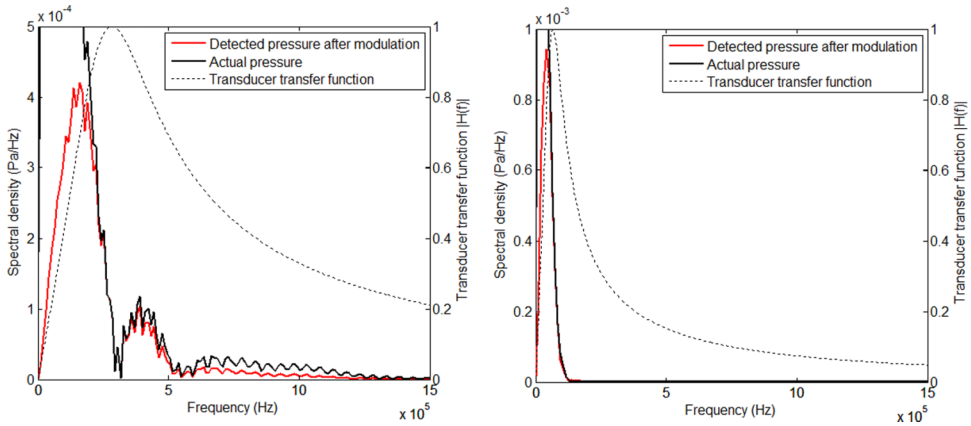

FIG. 3. Spectrum of acoustic waveforms at a detector 4 cm from the Bragg peak of the proton beam. The beam had a 100-MeV energy and a 1-mm spot size. Left: spectrum for a beam with a 0.1-μs pulse width. Right: spectrum for a beam with a 10-μs pulse width. The dotted line is the magnitude of the transfer function of the transducer. Actual pressure refers to the spectrum detected by an ideal noiseless detector with infinite bandwidth. Detected pressure refers to the spectrum measured by the realistically modeled transducer.

TABLE I. Minimum detection requirements for 100 MeV beams (Bragg peak depth: 7.5 cm).

Beam energy (MeV)	Pulse width (μs)	Spot size (mm)	Central frequency (kHz)	Noise equivalent pressure (mPa)	Minimum detectable dose (mGy)	Minimum protons per pulse	Required beam current (nA)
100	0.1	1	326	26	235	3.1×10^6	5000
100	0.1	5	302	26	41	3.6×10^6	5700
100	0.1	10	302	25	20	4.9×10^6	7800
100	1	1	300	25	253	3.4×10^6	540
100	1	5	207	21	32	2.8×10^6	450
100	1	10	213	21	17	4.0×10^6	650
100	5	1	128	17	376	5.0×10^6	160
100	5	5	125	17	61	5.3×10^6	170
100	5	10	131	17	39	9.4×10^6	300
100	10	1	76	13	647	8.6×10^6	140
100	10	5	73	13	94	8.1×10^6	130
100	10	10	76	13	69	1.7×10^7	270

to the decreased density of deposited energy which directly relates to the initial pressure. On the other hand, the minimum detectable dose is largest for the smallest spot size, because the dose at the Bragg peak is higher compared to a larger spot size for a fixed proton number.

The required dose versus pulse width has a more complicated relation. As the pulse width increases, the signal amplitude decreases, which also decreases the SNR; however, the signal is also contained within lower frequencies and the reduced noise over a lower bandwidth partially offsets the reduction in SNR. We observed that required dose decreased with increasing pulse width for the 100 MeV beam, but increased initially for the 160 MeV beam.

4. DISCUSSION

To assess whether the above simulation results are reasonable, we compare them to existing experimental measurements in similar irradiation scenarios. Sulak *et al.*[5] measured the proton-acoustic signal amplitude in a water phantom for a 158 MeV beam with a 10-mm spot size and 50-μs pulse width. In their measurement, the detector was placed 8 cm distal to the Bragg peak. The signal amplitude was measured for different proton numbers (Sulak, Fig. 17), and it was found that the linear relationship between these variables was approximately 0.9 dyne/cm^2 pressure per 10^{17} eV energy deposition, which equates to 9×10^{-18} Pa/eV. The closest corresponding situation in our simulations was the 160 MeV beam with a 10-mm spot size and 10-μs spill time (Table II, row 16). The central frequency of the simulation result was 69 kHz which is close to experimental result. The signal amplitude was 48 mPa (25 mPa noise-equivalent pressure times SNR = 4) for 1.7×10^7 protons. This equates to 1.6×10^{-17} Pa/eV peak pressure at detector per total energy deposition. Adjusting for the measurement distance from 4 to 8 cm, the acoustic amplitude is 7.9×10^{-18} Pa/eV (simulation 12% lower than experiment). The smallest signal detected in the Sulak study was with a 2×10^{16} eV energy deposition, whereas we predicted the detectability limit at 4.9×10^{15} eV energy deposition (4.1 times lower). Despite

TABLE II. Minimum detection requirements for 160 MeV beams (Bragg peak depth: 17.2 cm).

Beam energy (MeV)	Pulse width (μs)	Spot size (mm)	Central frequency (kHz)	Noise equivalent pressure (mPa)	Minimum detectable dose (mGy)	Minimum protons per pulse	Required beam current (nA)
160	0.1	1	381	28	796	2.4×10^7	39 000
160	0.1	5	353	27	147	2.1×10^7	34 000
160	0.1	10	346	27	81	3.1×10^7	49 000
160	1	1	295	25	734	2.2×10^7	3 600
160	1	5	283	24	117	1.7×10^7	2 700
160	1	10	276	24	65	2.4×10^7	3 900
160	5	1	98	15	288	8.8×10^6	280
160	5	5	94	14	46	6.7×10^6	220
160	5	10	97	15	33	1.2×10^7	390
160	10	1	67	12	410	1.3×10^7	200
160	10	5	65	12	62	9.0×10^6	150
160	10	10	67	12	51	1.9×10^7	300

the high beam current at their research facility, the sensitivity in the experimental study seems to have been somewhat limited by electrical noise (a noise source not included in our simulation). The authors noted that they "could not eliminate the electrical noise associated with the cyclotron generator."

Tada *et al.*[7] measured the proton-acoustic signal in a water phantom for a beam with a 51-mm range (approximately 7 cm d_{max}, 103-MeV energy), 10×10 cm field size, and 50-ns pulse width. The measurement location was approximately 4.5 cm distal to the Bragg peak. The closest corresponding situation in our simulations was the 100 MeV beam with a 10-mm spot size and 0.1-μs spill time (Table I, row 3). Tada *et al.* measured a 0.12 Pa amplitude for a beam delivering 4 mGy/pulse at the Bragg peak which corresponds to 2.2×10^{-17} Pa/eV pressure per total energy deposition. In our study, the signal amplitude was 100 mPa for 4.9×10^{6} protons and 20 mGy/pulse dose. This equates to 2.0×10^{-16} Pa/eV pressure per total energy deposition. The difference between the experiment and our simulation may be explained by the difference between the two field sizes. The acoustic wave fronts from different lateral parts of the Bragg peak do not always interfere constructively as they would for a smaller spot size. As a consequence, the experimental value of pressure/energy deposition is expected to be smaller. The Tada study did not report a measured sensitivity. Our predicted detectability limit was 20 mGy/pulse which is larger than the 4 mGy/pulse dose rate in the Tada study. This five-fold difference suggests that the authors must have had to average together at least 25 pulses. The authors noted that "the detected signals were noisy which necessitated averaging them over hundreds of pulses." Our results of signal amplitudes and sensitivity appear to agree reasonably well with the Sulak and Tada studies.

More recently, the study by Assmann *et al.*[16] demonstrated a clear proton-acoustic signal with an energy deposition as low as 10^{12} eV. In comparison, the energy deposition requirements in our simulations ranged from 0.6–9.6×10^{14} eV. This difference in detection limit arises from the substantial proton energy difference. This experimental study used a 20 MeV proton beam, which has a 4 mm range in water, whereas in our simulations the energies are 100 and 160 MeV. At 20 MeV, the beam has a very sharp Bragg peak of only 0.3 mm, which leads to a sharp proton-acoustic pulse. In addition, the pulses were averaged over 16 events for noise reduction. In addition to the lower required dose in that study, the small irradiation volume produced higher frequency acoustic signals up to 13.5 MHz, which theoretically allows a spatial resolution of 55 μm. For more clinically relevant proton energies, the minimum detectable dose and spatial resolution scale as indicated by our simulations.

We have tabulated the minimum dose and beam currents required to detect a *single* pulse. The previous experiments on the proton-acoustic method mainly used high beam current research facilities. In practice, the maximum beam current available at clinical proton therapy facilities is about 300 nA. As seen in Tables I and II, several of the simulation scenarios require a beam current lower than 300 nA, indicating feasibility. However, this does not impose an absolute limit on beams with lower pulse intensities. Random noise, including thermal noise, can be mitigated by averaging the proton-acoustic signal over multiple pulses. In fact, this strategy was used in the Tada and Assmann studies. The effective noise decreases by a factor of $\sqrt{N}$, where N is the number of pulses. For example, the detection limit for the 5-mm spot size, 5-μs pulse width, 100-MeV beam is 9 mGy (25.6 nA beam current). An irradiation with half the pulse intensity (4.5 mGy, 12.8 nA current) can be detected by averaging the acquired waveform over four pulses. The total dose required for detection is then 4.5 mGy × 4 = 18 mGy. The results in Tables I and II are therefore applicable to proton beams with lower proton numbers/beam currents than those indicated here; the total dose and number of averages must be adjusted accordingly.

In this study, we considered only the thermal noise in the transducer piezo material as this is the main source of noise in this application. Other sources of noise include thermal noise in the patient, electronic noise, as well as electromagnetic interference. The latter is not a random noise source, and instead is often temporally correlated with the acoustic signal. In this case, careful electronic shielding may be needed to isolate the acoustic detection system from this interference.

Sulak *et al.* state that sensitivity of hydrophones can approach $N_0 = 6\times10^{-7}$ Pa/$\sqrt{\text{Hz}}$ which is 42 times lower (better) than that calculated for the PZT transducer in these simulations. These detectors are likely much larger than the 5-cm diameter hydrophone in our simulation, and would have lower transducer noise. In principle, the required doses should be 42 times lower with the best available hydrophones than in this study. On the other hand, this improvement would also be partially offset because the acoustic pulse reaches different parts of the detector at different times. Nevertheless, this detection strategy may be one way of reducing the noise and increasing the sensitivity of proton-acoustic detection.

Although we considered a single transducer in this simulation study, signal from multiple detectors can be combined to reduce noise and increase the sensitivity of this method. This would require precise calibration of time-of-flight to the multiple detectors. The Bragg peak must also be within the received focal spot of the multiple detectors.

A common clinical situation that we did not consider is treatment using a spread-out Bragg peak (SOBP) to cover large targets, i.e., wider than the width of a pristine Bragg peak. Although we did not explicitly investigate this situation, the many pulses within a SOBP can be treated separately in time because this technique responds to irradiation on a pulse-by-pulse basis. The localization of the SOBP can be achieved by monitoring all the pulses that contribute to a SOBP.

5. CONCLUSION

Proton-acoustic range verification has been simulated and the detection limits of this method have been determined. An analytical model was used to calculate the initial pressure distribution from a single pulse. A finite element solver

was used to find numerical solution of the general wave equation and calculate the resulting acoustic waves from the initial pressure. A realistic noise model was used to simulate noise, and thus a realistic SNR, in the simulations. The proton-acoustic model was evaluated in simulations using two different proton energies, representing different clinical scenarios. Other simulation parameters included pulse widths, beam energy, and spot sizes. The detection limits, in terms of noise, minimum dose per pulse, and number of protons have been tabulated for irradiations with various values of the simulation parameters. The required doses ranged from 2 to 117 mGy/pulse corresponding to $0.6–6\times10^6$ protons/pulse. The signal-to-noise ratio can be further improved by increasing the number of pulse averages, which would be a step toward clinical applicability. The ultrasound frequencies ranged from 65 to 385 kHz. Ultrasound frequency decreases with proton beam pulse width with pulses wider than 10-μs producing signal below 100 kHz, which may degrade the precision of range verification.

ACKNOWLEDGMENTS

We would like to thank Taeko Matsuura, Seishin Takao, Hiroki Shirato, Kikuo Umegaki, and the staff of the Hokkaido University Hospital, Proton Beam Therapy Center for helping us understand the instrumentation and experimental setup in proton-acoustic measurement and for their very valuable discussion. We also wish to acknowledge the support from the NCI (Nos. 1R01 CA176553 and R25T CA118681).

APPENDIX: ANALYSIS OF ELECTRICAL NOISE

In this Appendix, we analyze the impact of electrical noise to the acoustic measurement. In particular, we seek to estimate the noise added by the amplifier circuit to the measured acoustic signal. This problem has been studied previously by Yañez *et al.* and we apply their approach[23] for our particular transducer and frequency range. A simple noninverting operational amplifier (op-amp) circuit is shown in Fig. 4. The transducer is modeled as an input voltage source Vs with an electrical impedance Zs. V_0 is the amplified signal output. The noise in the output V_0 comes from: the transducer (random variations in Vs); the op-amp; and the resistors $R1$ and $R2$. By modeling the noise in each of the circuit elements in Fig. 4, we obtain the following noise equivalent circuit in Fig. 5.

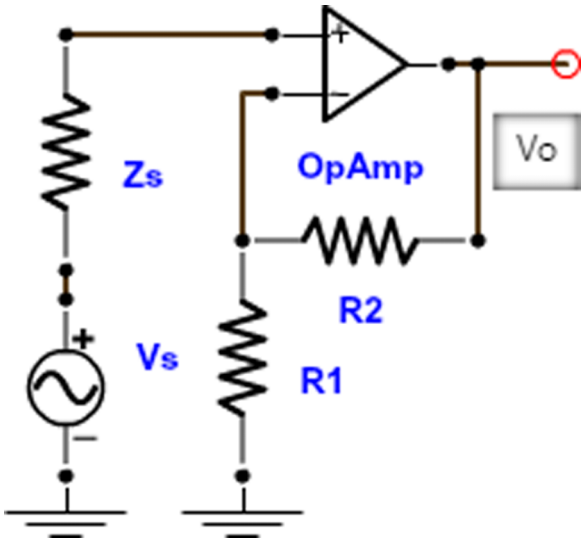

FIG. 4. Schematic of the non-inverting amplifier. The transducer is modeled as an input voltage source Vs with an electrical impedance Zs. V_0 is the amplified signal output.

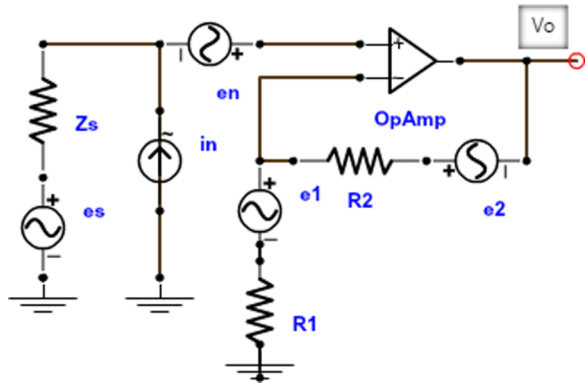

FIG. 5. Noise equivalent hydrophone amplifier circuit.

Using the definition of capacitance and the formula $f_{\max} = 0.44 c_l/l$, [Ref. 14, Eq. (5)] the capacitance of the transducer in this study can be calculated as

$$C = \frac{\epsilon\epsilon_0 A}{l} = 2.27\frac{\epsilon\epsilon_0 A}{c_l} f_{\max} = 2.8\,\text{nF}.$$

We used the values of $\epsilon\epsilon_0$, c_l of PZT-5 taken from Oraevsky *et al.*, area $A = 20$ cm^2, and a frequency of $f_{\max} = 100$ kHz, which is typical of the signals in this study. The transducer impedance is calculated as $Z_s = |1/j\omega C|$, where $\omega = 2\pi f$ is the angular frequency. Using $f = 100$ kHz, we calculate a transducer impedance of $Z_s = 568\,\Omega$. In Fig. 5, the transducer has been replaced with a voltage noise source e_n, and an impedance $Z_s = 7.6\,\Omega$. We have already calculated a noise-equivalent pressure density of $N_0 = 2.7\times10^{-5}$ Pa/$\sqrt{\text{Hz}}$. To convert to voltage noise, we multiply by the transducer gain gl. Using Eq. (6), we obtain

$$e_s = N_0 \cdot gl = \sqrt{\frac{4kT}{Cf_{\max}}} = 7.66\,\text{nV}/\sqrt{\text{Hz}}.$$

TABLE III. Noise specifications of common low-noise amplifier integrated circuits.

Manufacturer	Model	Voltage noise e_n $\left(\text{nV}/\sqrt{\text{Hz}}\right)$	Current noise i_n $\left(\text{fA}/\sqrt{\text{Hz}}\right)$
Texas Instruments	OPA847	0.85	2500
Maxim	MAX4106	0.75	2500
Texas Instruments	LMH6624	0.92	2300
Texas Instruments	CLC425	1.05	1600
Texas Instruments	OPA657	4.8	1.3

TABLE IV. Amplitude of noise in the various electrical components of the amplifier circuit. V_0 is the overall noise at the amplifier output.

Amplifier	$e_n\left(\text{nV}/\sqrt{\text{Hz}}\right)$	$e_s\left(\text{nV}/\sqrt{\text{Hz}}\right)$	$\lvert Z_S\rvert i_n\left(\text{nV}/\sqrt{\text{Hz}}\right)$	$e_1\left(\text{nV}/\sqrt{\text{Hz}}\right)$	$R_2 i_n\left(\text{nV}/\sqrt{\text{Hz}}\right)$	V_0 (mV)
OPA847	0.85	7.66	1.42	0.29	1.24	0.25
MAX4106	0.75	7.66	1.42	0.29	1.24	0.25
LMH6624	0.92	7.66	1.31	0.29	1.14	0.25
CLC425	1.05	7.66	0.91	0.29	0.79	0.25
OPA657	4.80	7.66	7.4×10^{-4}	0.29	6.4×10^{-4}	0.29
Ideal	0	7.66	0	0	0	0.24

The op-amp has an internal voltage noise e_n and a current noise i_n. In Table III, we have listed several op-amp integrated circuits with their nominal values of e_n and i_n. Note that most values of e_n are nearly one order-of-magnitude lower compared to e_s. This is a hint that electronic noise will be negligible compared to transducer noise. The gain of the amplifier circuit is set by the values of the resistors $R1$ and $R2$ and is equal to $G = 1 + R2/R1$. We set an amplifier gain of 100 using $R1 = 5\ \Omega$, $R2 = 495\ \Omega$. $R1$ is kept as reasonably low as possible to minimize resistor thermal noise, but still high enough to be greater than stray resistance (conductors, wires, solder joints) in the circuit. Resistors $R1$ and $R2$ each carry a voltage noise equal to $\sqrt{4kTR}$.

Yanes *et al.* have derived the expression for the output noise density of this amplifier configuration,

$$v_0^2 = G^2\left(e_n^2 + e_s^2 + |Z_s|^2 i_n^2 + e_1^2\right) + R_2^2 i_n^2, \tag{A1}$$

$$V_0 = v_0\sqrt{\text{BW}}. \tag{A2}$$

V_0 is the overall noise at the amplifier output and is obtained by multiplying v_0 with the signal bandwidth. We chose a bandwidth of 100 kHz as it is representative of the signals studied in this work. The output noise when all noise sources except the transducer are turned off is $G^2 e_s^2$. This corresponds to the situation the transducer signal is amplified by an ideal noiseless amplifier. We have listed the overall noise values for the five op-amp IC circuits and the ideal noiseless amplifier in Table IV. The largest noise source is e_s, the transducer itself. The next significant noise sources are the amplifier current noise loaded by the transducer impedance and the amplifier voltage noise, $|Z_S| i_n$ and e_n, respectively. The noise in the $R2$ resistor $R_2 i_n$ has very little impact since it is not multiplied by the op-amp gain.

The noise at the output of the ideal noiseless amplifier is 0.24 mV, whereas in the selected real amplifier circuits it is between 0.25 and 0.29 mV. Clearly, the noise from the amplifier circuit is much lower than the noise contribution from the transducer itself.

This analysis shows that electronic noise is not necessarily the limiting factor in proton-acoustic measurements. We considered five different commercially available low-noise amplifier IC packages. To achieve this noise minimum in practice, the amplifier circuit should be placed as close to the transducer as possible. This requires integration of the amplifier directly into the hydrophone assembly. This approach amplifies the signal before the hydrophone cable and thus minimizes the impact of stray signals picked up by the cable.

[a]Author to whom correspondence should be addressed. Electronic mail: lei@stanford.edu; Telephone: 650-724-8288.

[1]A. J. Lomax, "Intensity modulated proton therapy and its sensitivity to treatment uncertainties 1: The potential effects of calculational uncertainties," Phys. Med. Biol. **53**(4), 1027–1042 (2008).
[2]K. Parodi, W. Enghardt, and T. Haberer, "In-beam PET measurements of β^+ radioactivity induced by proton beams," Phys. Med. Biol. **47**(1), 21–36 (2002).
[3]C.-H. Min, C. H. Kim, M.-Y. Youn, and J.-W. Kim, "Prompt gamma measurements for locating the dose falloff region in the proton therapy," Appl. Phys. Lett. **89**(18), 183517 (2006).
[4]S. W. Peterson, D. Robertson, and J. Polf, "Optimizing a three-stage Compton camera for measuring prompt gamma rays emitted during proton radiotherapy," Phys. Med. Biol. **55**(22), 6841–6856 (2010).
[5]L. Sulak *et al.*, "Experimental studies of the acoustic signature of proton beams traversing fluid media," Nucl. Instrum. Methods **161**(2), 203–217 (1979).
[6]G. A. Askariyan, B. A. Dolgoshein, A. N. Kalinovsky, and N. V. Mokhov, "Acoustic detection of high energy particle showers in water," Nucl. Instrum. Methods **164**(2), 267–278 (1979).
[7]J. Tada, Y. Hayakawa, K. Hosono, and T. Inada, "Time resolved properties of acoustic pulses generated in water and in soft tissue by pulsed proton beam irradiation—A possibility of doses distribution monitoring in proton radiation therapy," Med. Phys. **18**(6), 1100–1104 (1991).
[8]N. A. Baily, "A review of the processes by which ultrasound is generated through the interaction of ionizing radiation and irradiated materials: Some possible applications," Med. Phys. **19**(3), 525–532 (1992).
[9]Y. Hayakawa *et al.*, "Acoustic pulse generated in a patient during treatment by pulsed proton radiation beam," Radiat. Oncol. Invest. **3**(1), 42–45 (1995).
[10]L. Xiang, B. Han, C. Carpenter, G. Pratx, Y. Kuang, and L. Xing, "X-ray acoustic computed tomography with pulsed x-ray beam from a medical linear accelerator," Med. Phys. **40**(1), 010701 (5pp.) (2013).
[11]M. Xu and L. V. Wang, "Photoacoustic imaging in biomedicine," Rev. Sci. Instrum. **77**(4), 041101 (2006).
[12]K. C. Jones, A. Witztum, C. M. Sehgal, and S. Avery, "Proton beam characterization by proton-induced acoustic emission: Simulation studies," Phys. Med. Biol. **59**(21), 6549–6563 (2014).
[13]F. Alsanea, V. Moskvin, and K. M. Stantz, "Feasibility of RACT for 3D dose measurement and range verification in a water phantom," Med. Phys. **42**(2), 937–946 (2015).
[14]K. Stantz, F. Alsanea, and V. Moskvin, "TH-C-144-01: Best in physics (THERAPY)—Use of radiation-induced ultrasound to image proton dosimetry," Med. Phys. **40**(6), 546 (2013).
[15]F. Alsanea, V. Moskvin, and K. Stantz, "SU-E-CAMPUS-T-02: Exploring radiation acoustics CT dosimeter design aspects for proton therapy," Med. Phys. **41**(6), 382 (2014).
[16]W. Assmann *et al.*, "Ionoacoustic characterization of the proton Bragg peak with submillimeter accuracy," Med. Phys. **42**(2), 567–574 (2015).
[17]A. A. Oraevsky and A. A. Karabutov, "Ultimate sensitivity of time-resolved optoacoustic detection," Proc. SPIE **3916**, 228–239 (2000).

[18]A. M. Winkler, K. Maslov, and L. V. Wang, "Noise-equivalent sensitivity of photoacoustics," J. Biomed. Opt. **18**(9), 097003 (2013).
[19]E. Pedroni *et al.*, "Experimental characterization and physical modelling of the dose distribution of scanned proton pencil beams," Phys. Med. Biol. **50**(3), 541–561 (2005).
[20]R. S. Dingus and R. J. Scammon, "Grüneisen-stress-induced ablation of biological tissue," Proc. SPIE **1427**, 45–54 (1991).
[21]B. E. Treeby and B. T. Cox, "k-Wave: MATLAB toolbox for the simulation and reconstruction of photoacoustic wave fields," J. Biomed. Opt. **15**(2), 021314 (12pp.) (2010).
[22]A. Rose, *Vision* (Springer US, Boston, MA, 1974).
[23]Y. Yañez, M. J. Garcia-Hernandez, J. Salazar, A. Turo, and J. A. Chavez, "Designing amplifiers with very low output noise for high impedance piezoelectric transducers," NDT&E Int. **38**(6), 491–496 (2005).